Chapter 6

Experimental Data Deconvolution Based on Fourier Transform Applied in Nanomaterial Structure

Adrian Bot, Nicolae Aldea and Florica Matei

Additional information is available at the end of the chapter

http://dx.doi.org/10.5772/59667

1. Introduction

In many kinds of experimental measurements, such as astrophysics, atomic physics, biophysics, geophysics, high energy physics, nuclear physics, plasma physics, solid state physics, bending or torsion elastic, heat propagation or statistical mechanics, the signal measured in the laboratory can be expressed mathematically as a convolution of two functions. The first represents the resolution function called the instrumental signal, which is specific for each setup, and the second is the true sample that contains all physical information. These phenomena can be modelled by an integral equation, which means the unknown function is under the integral operator. The most important type of integral equation applied in physical and technical signal treatments is the Fredholm integral equation of the first kind. The opposite process when used for true sample function determination is known in the literature as experimental data deconvolution. Solution determination of the deconvolution equation does not readily unveil its true mathematical implications concerning the stability of the solutions or other aspects. Thus, from this point of view, the problem is described as improper or ill-posed. The most rigorous methods for solving the deconvolution equation are: regularization, spline function approximation and Fourier transform technique. The essential feature of regularization method is the replacement of a given improper problem with another, auxiliary, correctly posed problem. The second method consists in approximating both the experimental and instrumental signals by piecewise cubic spline. Most often when using this technique, the true sample function belongs to the same piecewise cubic spline class. The topic of this chapter is the application of Fourier transform in experimental data deconvolution for use in nanomaterial structures.

2. Mathematical background of signal deconvolution

As mentioned in the introduction, ill-posed problems from a mathematical point of view have many applications in physics and technologies [1]. In addition to the abovementioned examples, the examples below should be noted.

Solving the Cauchy problem for the Laplace equation, $\Delta U = 0$ has a direct application in biophysics as in [2]. The problem consists in determining the biopotential distribution within the body denoted by U, when the body surface potential values are known. The phenomenon is modelled by the Laplace equation, and the Cauchy conditions are $U|_S = f(S)$ and $\frac{\partial U}{\partial n}\Big|_S = 0$, where S represents the surface of the body.

The determination of radioactive substances in the body, as in [2], and protein crystallography structures also deal with ill-posed problems: see [3].

The same formalism is used in quantum mechanics to determine the particle scattering cross-section on different targets, as well as in plasma physics in the case of the electron distribution after speed is received from the dispersion curve analysis [2].

An intuitive way of grasping an ill-posed problem can be modelled by the movement of the vibrating string when many forces are acting perpendicularly on the string, as represented in Figure 1.

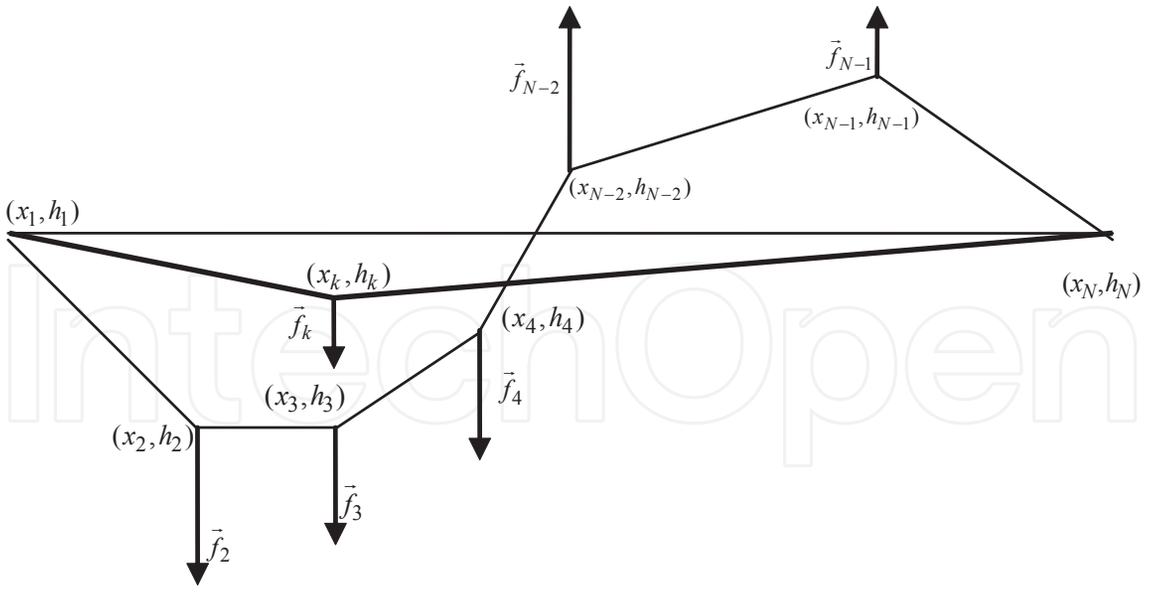

Figure 1. Physical model of the vibrating string

In terms of the mathematical equation, the phenomenon described above has a correspondent in physics spectroscopy used in the study of nanomaterials. In the first instance, it is considered that in the point of abscissa x_k, force $\vec{f}_k$ acts perpendicularly to the direction of the string. The

http://dx.doi.org/10.5772/59667

string movement in the vertical plane at an arbitrary point s is given by the proportionality relationship,

$$h(s) = g(s, x_k) f(x_k) \tag{1}$$

where $g(s, x_k)$ characterizes the impact of force $\vec{f}(x_k)$ on the movement $h(s)$. Using the same considerations, for N forces $\vec{f}_1, \vec{f}_2, \cdots, \vec{f}_N$ that act independently in N points of abscissa x_1, x_2, ..., x_N in the direction perpendicular to the string, the string movements will be obtained as $h_1, h_2, ..., h_N$. Therefore the movement associated with an arbitrary point of the string of abscissa s is described by the relation below

$$h(s) = g(s, x_1) f(x_1) + g(s, x_2) f(x_2) + \cdots + g(s, x_k) f(x_k) = \sum_{i=1}^{N} g(s, x_k) f(x_k) \tag{2}$$

When a force is distributed continuously along the entire string, the movement of the point s of the string will be given by

$$h(s) = \int_0^l g(s, x) f(x) dx \tag{3}$$

where l represents the length of the string.

The function f is the density of force, which means the force per unit length, and $f(x)dx$ represents the force that acts on the arc element dx. The function g is called the influence function because it shows the degree of influence of the distribution force f on displacement h.

The equation (3) is named the Fredholm integral equation of the first kind, and it is a particular case of the integral equation,

$$l(s) f(s) + \int_a^b g(s, x) f(x) dx = h(s), \quad c \le x \le d \tag{4}$$

where l, g and h are continuous known functions. If function l is null, then equation (4) represents an integral equation of the first kind. If function l has no zero on $[c, d]$ then the equation (4) is of the second kind, while if l has some zeros on $[c,d]$ then the equation (4) is of the third kind.

Although the aim of this chapter is signal deconvolution using the Fourier transform, it is important to mentionthe other two methods used to solve equation (4) when $l \equiv 0$, that is, the regularization method and the spline approach.

Hadamard stated that a problem is well posed if it has a unique solution, and the solution depends continuously on the data [4]. Any problem that is not a well-posed problem is an ill-posed one. The Fredholm equation of the first kind is ill posed because small changes in the data generate huge modification of the unknown function.

2.1. Regularization method

This method consists in the replacement of the ill-posed problem (4) with $l \equiv 0$ by a well-posed problem, and there are many scientific papers that develop different types of regularization method depending on kernel type and other specific needs. Below we describe the Tikhonov regularization method applied to the equation (4) with $l \equiv 0$. Let X and Y be Hilbert spaces and $\|\cdot\|$ be the norm on Hilbert space. If the kernel g is smooth, the operator $G: X \to Y$

$$(Gf)(s) = \int_a^b g(s,x) f(x) dx \tag{5}$$

is linear. Then equation (4) with $l \equiv 0$ becomes

$$Gf = h \tag{6}$$

The regularization method consists in the determination of the approximate solution of the equation (4) of the first kind as a minimization of the following functional

$$\Phi_a(f) = \|G - h\|^2 + \alpha \|Lf\|^2, \forall f \in X \tag{7}$$

The value $\alpha > 0$ represents the regularization parameter and L is a linear operator defined below

$$Lf = a_0(f - \hat{f}) + a_1 f' + a_2 f'' \tag{8}$$

where a_i has the value 0 or 1; and f' and f'' are the first and the second derivative of f. Function $\hat{f}$ represents a trial solution for equation (4) with $l \equiv 0$. The regularization order for the operator L is the same as the derivability order of f. The regularization parameter should be chosen carefully, because a good minimum for the functional (7) does not always lead to an adequate solution for equation (4) with $l \equiv 0$ as in [4]. The discrimination procedure of the equation (4) with $l \equiv 0$ and functional (7) depends on the specifics of each type of problem such as domain, type of kernel, etc., but this is not the subject of this chapter: see [4-6].

Some disadvantages of the regularization method, which is an iterative method, are the fact that it is very sensitive to the noise present in the experimental function and is time consuming.

http://dx.doi.org/10.5772/59667

If the kernel g of the equation (4) with $l \equiv 0$ has a delayed argument then the equation is called a convolution equation, and is widely applied in physical spectroscopy. The general form of a convolution equation is given by

$$h(s) = \int_{-\infty}^{\infty} g(s-x) f(x) dx \tag{9}$$

After the change of variable $x=t-s$ it is found that (9) is equivalent by the equation

$$h(s) = \int_{-\infty}^{\infty} g(t) f(t-s) dt \tag{10}$$

2.2. Spline technique

Spline functions for signal deconvolution technique help eliminate the drawbacks mentioned above [7]. The advantage of the method proposed in [7] lies in the fact that Beniaminy's method is a one-step method. In this case, the true sample function f is represented as a piecewise cubic spline function, and after the substitution of it into equation (10), the experimental function h becomes a piecewise cubic spline function with the same knots but different coefficients. The connection between the coefficients of functions h and f are given by the moments of instrumental function g. Thus, if function f has the form

$$f(t) = \sum_{k=1}^{n-1} s_k(t) \tag{11}$$

where

$$s_k(t) = \begin{cases} 0 & \text{if} \quad t < \xi_k \\ a_k t^3 + b_k t^2 + c_k t + d_k & \text{if} \quad \xi_k \le t \le \xi_{k+1} \\ 0 & \text{if} \quad \xi_{k+1} < t \end{cases} \tag{12}$$

with ξ_k, $k=\overline{1,\ n-1}$ are the knots and a_k, b_k, c_k and d_k are the coefficients of the spline function f. They are chosen such that the function together with its first two derivatives is continuous. Replacing (12) in (11), the experimental function has the form

$$h(s) = \sum_{k=1}^{n-1} \left(A_k t^3 + B_k t^2 + C_k t + D_k \right) \tag{13}$$

where

$$\begin{aligned} A_k &= a_k M_0 \\ B_k &= b_k M_0 - 3a_k M_1 \\ C_k &= 3a_k M_2 - 2b_k M_1 + c_k M_0 \\ D_k &= -a_k M_3 + b_k M_2 - c_k M_1 + d_k M_0 \end{aligned} \tag{14}$$

and $M_k = \int_{-\infty}^{\infty} t^k g(t)dt$ represents the moment of order k. Beniaminy considered that experimental function h given by (14) is a cubic spline function. In [8] it is shown that that function h is not a spline function due to the lack of the continuity in the first two derivatives of h. However, the algorithm from [7] gives good results, but the quality of the true sample function depends on how wide the instrumental function is. In order to obtain the true sample function f given by (12) and (13), we calculate spline coefficients of the experimental function and using these values and (14) obtain the coefficients a_k, b_k, c_k and d_k.

2.3. Solving the convolution equation using Fourier transform

Take the functions h, f, and g whose Fourier transform is given by the functions H, F and G. By applying the Fourier transform operator on both members of equation (10) we obtain

$$\int_{-\infty}^{+\infty} h(s)\exp(-2\pi i\nu s)ds = \int_{-\infty}^{+\infty}\left[\int_{-\infty}^{+\infty} g(\tau)f(s-\tau)d\tau\exp(-2\pi i\nu s)\right]ds \tag{15}$$

By changing the order of integration, the Fourier transform of the signal h is expressed by the relation,

$$H(\nu) = \int_{-\infty}^{+\infty} g(\tau)\left[\int_{-\infty}^{+\infty} f(s-\tau)\exp(-2\pi i\nu s)ds\right]d\tau \tag{16}$$

Using the substitution $\sigma = s - \nu$, the quantity between square brackets from the previous relation becomes

$$\int_{-\infty}^{+\infty} f(\sigma)\exp\left[-2\pi i\nu(\sigma+\tau)\right]d\sigma = \exp(-2\pi i\nu\tau)\int_{-\infty}^{+\infty} f(\sigma)\exp(-2\pi i\nu\sigma)d\sigma = \exp(-2\pi i\nu\tau)F(\upsilon) \tag{17}$$

In this context the relation (16) becomes

$$H(\nu) = \int_{-\infty}^{+\infty} g(\tau)\exp(-2\pi i\nu\tau)F(\nu)d\tau = F(\nu)G(\nu) \tag{18}$$

http://dx.doi.org/10.5772/59667

The relation (18) is known as the convolution theorem. If direct and inverse Fourier transform operators and convolution product are respectively denoted by TF, TF^{-1} and *, then the relation (18) is written symbolically as

$$TF(h) = TF(f)TF(g) = F\,G = TF(f * g)$$

and

$$TF^{-1}(F\,G) = h = f * g$$

In this way, the process of the inverse Fourier transform applied to function F determines f signal. In X-ray diffraction theory this is known as the Stokes method.

Experimental signals h, coded by (1), (3), (5) and (6) for a set of supported gold catalyst (Au/SiO_2), and instrumental contribution g measured on a gold foil, are presented in Figure 2.

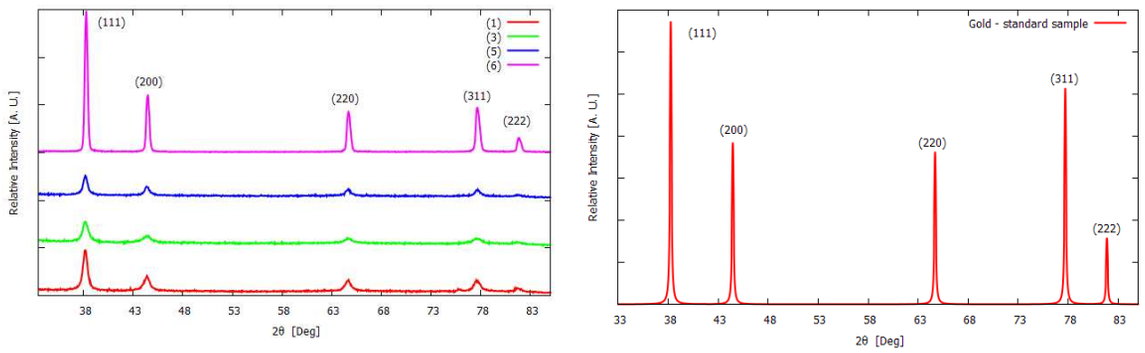

Figure 2. The experimental relative intensities h of the supported gold catalysts and instrumental function g

3. Why is the technique of deconvolution used in nanomaterials science?

In the scientific literature we can see many authors display serious confusion about the concept of deconvolution. Often, when they decompose the experimental signal h according to certain specific criteria, some say that it has achieved the deconvolution of the initial signal. This fact may be accepted only if the instrumental function g from equation (11) is described by the Dirac distribution. Only in this case is the true sample function f identical to the experimental signal h. Unfortunately, no instrumental function of any measuring device can be described by the Dirac distribution.

It is well known that the macroscopic physical properties of various materials depend directly on their density of states (DS). The DS is directly linked to crystallographic properties. For physical systems that belong to the long order class, moving the crystallographic lattice in the

whole real space will reproduce the whole structure. The nanostructured materials, which belong to the short-range class, are obtained by moving the lattice in the three crystallographic directions at the limited distances, generating crystallites whose size is no greater than a few hundred angstroms. In this case, the DS is drastically modified in comparison with the previous class of materials. From a physical point of view the DS is closely related to the nanomaterials' dimensionality, so crystallite size gives direct information about new topological properties. It can emphasize that amorphous, disordered or weak crystalline materials can have new bonding and anti-bonding options. The systems consisting of nanoparticles whose dimensions do not exceed 50 Å have the majority of atoms practically situated on the surface for the most part. Additionally, the behaviour of crystallites whose size is between 50 Å and 300 Å is described on the basis of quantum mechanics to explain the advanced properties of the tunnelling effect. All these reasons lead to the search for an adequate method to determine reliable information such as effective particle size, microstrains of lattice, and particle distribution function. This information is obtained by Fourier deconvolution of the instrumental and experimental X-ray line profiles (XRLP) approximated by Gauss, Cauchy and Voigt distributions and generalized by Fermi function (GFF) as in [9]. The powder reflection broadening of the nanomaterials is normally caused by small size, crystallites and distortions within crystallites due to dislocation configurations. It is the most valuable and cheapest technique for the structural determination of crystalline nanomaterials.

Generally speaking, in X-ray diffraction on powder, the most accurate and reliable analysis of the signals is given by the convolution equation (10) where *h*, *g* and *f* are experimental data, instrumental contribution of setup experimental spectrum, and true sample function as a solution of equation (10), respectively.

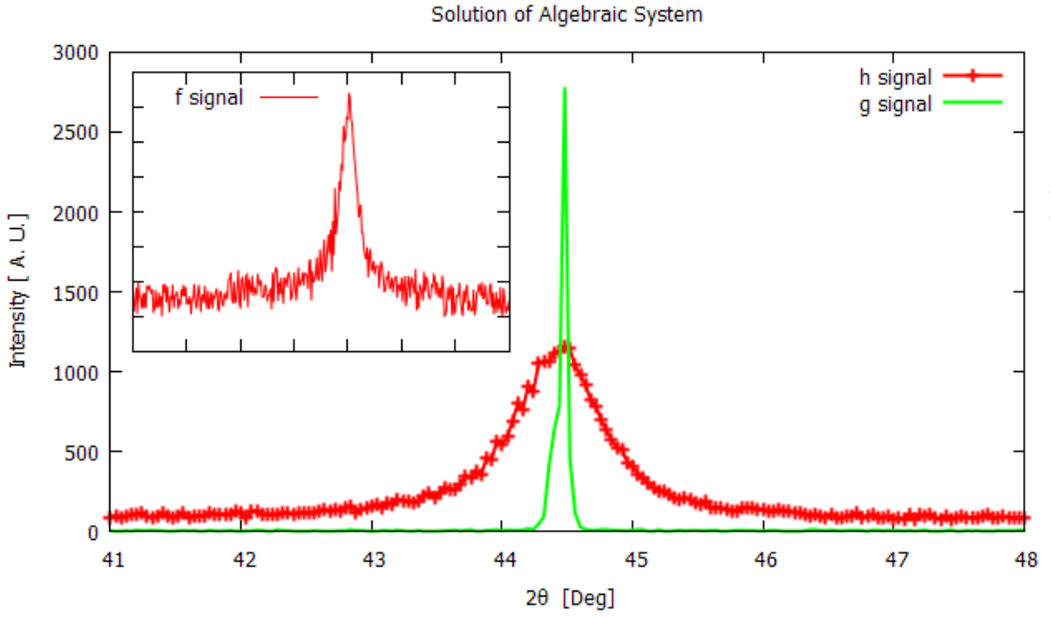

Figure 3. Numerical solution of the deconvolution equation (19) determined by an algebraic discretization

http://dx.doi.org/10.5772/59667

Let us consider the experimental signals of (111) X-ray line profile of supported nickel catalyst, and the instrumental function given by nickel foil obtained by a synchrotron radiation setup at 201 points with a constant step of 0.04^0 in 2θ variables, as shown in Figure 3.

The convolution equation (9) can be approximated in different ways, but the simplest approximation is given by following the algebraic system

$$h(x_i) = \sum_{j=-201}^{201} g(x_i - s_j) f(s_j) \Delta s_j \ldots i = 1,201 \tag{19}$$

where Δs_j is a constant step in 2θ variables. It turns out that the roots $f(s_j)$ of system (19) do not lead to a smooth signal, but yield a curve which makes for enhanced oscillations. Its behaviour is given by *f* signal in Figure 3. This result is given by a computer code written in Maple 11 language, a sequence of which is presented in Appendix 1. From a physical point of view, this type of solution is impracticable because the crystallite size in nanostructured systems is contained in the tails of XRLP. Therefore, the lobes of the XRLP must be sufficiently smooth. As shown in the inset of Figure 3, this condition is not met.. It would be possible to improve the quality of signal *f* trying to extend the definition interval for signal g. Thus we will approximate the unbounded integral on a bounded interval, but one that is sufficiently large.

This depends on the performances of the computer system and on the algorithm developed for solving inhomogeneous systems of linear equations with sizes of at least several thousand.

4. Distributions frequently used in physics and chemical signal deconvolution applied in nanomaterials science

It is known that, from a mathematical point of view, the XRLP are described by the symmetric or asymmetric distributions. As in [10,11] a large variety of functions for analysis of XRLP, such as Voigt (V), pseudo-Voigt (pV) and Pearson VII (P7), are proposed.

4.1. Gauss distribution

Many results such as the propagation of uncertainties and the least square method can be derived analytically in explicit form when the relevant variables are normally distributed. Gauss distribution is defined by mathematical relation

$$I_G = \frac{I_{0G}}{\sqrt{\pi}\gamma_G} \exp\left[-\left(\frac{x-a}{\gamma_G} \right)^2 \right] \tag{20}$$

where I_{0G}, *a* and γ_G are the profile area, gravitational centre measured in 2θ variable, and broadening of the XRLP, respectively. The n^{th} moment, n=0,1 is given by relations

$$\mu_{0G} = \int_{-\infty}^{+\infty} I_G(x)dx = I_{0G}, \qquad \mu_{1G} = a$$

The integral width δ_G and full width at half maximum $FWHM_G$ are given by relations

$$\delta_G = \sqrt{\pi}\gamma_G \quad \text{and} \quad FWHM_G = 2\sqrt{\ln 2}\gamma_G$$

If both signals *h* and *g* are described by Gaussian distributions and take into account the relationship (18), the full width and FWHM of the true sample function are expressed by the relations

$$\gamma_{G,f} = \sqrt{\gamma_{G,h}^2 - \gamma_{G,g}^2} \quad FWHM_{G,f} = 2\sqrt{\ln 2}\gamma_{G,f} \tag{21}$$

4.2. Cauchy distribution

The Cauchy distribution, also called the Lorentzian distribution, is a continuous distribution that describes population distribution of electron levels with multiple applications in physical spectroscopy. Its analytical expression is given by relation

$$I_C = \frac{I_{0C}}{\pi} \frac{\gamma_C}{\gamma_C^2 + (x-a)^2} \tag{22}$$

where I_{0C}, a and γ_C are profile surface, gravitational centre and broadening of the XRLP, respectively. The n^{th} moment n=0,1 is given by relations

$$\mu_{0C} = \int_{-\infty}^{+\infty} I_C(x)dx = I_{0C} \quad \text{and} \quad \mu_{1C} = a$$

The integral widths δ_G and full width at half maximum $FWHM_C$ are given by relations

$$\delta_C = \pi\gamma_C \quad \text{and} \quad FWHM_C = 2\gamma_C$$

The deconvolution of two signals h and g determined by Cauchy distributions is also a Cauchy distribution whose full width $\delta_{C,f}$ and $FWHM_{C,f}$ are given by relations

$$\delta_{C,f} = \delta_{C,h} - \delta_{C,g} \quad \text{and} \quad FWHM_{C,f} = 2\delta_{C,f} \tag{23}$$

http://dx.doi.org/10.5772/59667

4.3. Generalized Fermi function

Although extensive research over the past few decades has made progress in XRLP global approximations, their complete analytical properties have not been reported in the literature. Unfortunately, most of them have complicated forms, and they are not easy to handle mathematically. Recently, as in [9,11], a simple function with a minimal number of parameters named the generalized Fermi function (GFF), suitable for minimization and with remarkable analytical properties, was presented from a purely phenomenological point of view. It is given by the relationship,

$$h(s) = \frac{A}{e^{-a(s-c)} + e^{b(s-c)}} \tag{24}$$

where *A, a, b, c* are unknown parameters. The values *A, c* describe the amplitude and the position of the peak, and *a, b* control its shape. If *b=0*, the *h* function reproduces the Fermi-Dirac electronic energy distribution. The GFF has remarkable mathematical properties, with direct use in determining the moments, the integral width, and the Fourier transform of the XRLP, as well as the true sample function. Here we give its properties without proofs.

i. By setting

$$s' = s - c \quad \rho = (a+b)/2 \quad q = (a-b)/2$$

we obtain

$$h(s') = \frac{A}{2}\left(\frac{\cosh qs' + \sinh qs'}{\cosh \rho s'}\right) \tag{25}$$

ii. the limit of *h* function for infinite arguments is finite, so $\lim h(s') = 0$ when $s' \to \pm\infty$;

iii. the zero, first and second order moments (μ_0, μ_1, μ_2) of the *h* function are given by the relations

$$\mu_0 = \frac{\pi A}{2\rho \cos\frac{\pi q}{2\rho}}, \quad \mu_1 = \frac{\pi}{2\rho}\tan\frac{\pi q}{2\rho}, \quad \mu_2 = \left(\frac{\pi}{2\rho}\right)^2\left(\frac{1}{\cos^2\frac{\pi q}{2\rho}} + \tan^2\frac{\pi q}{2\rho}\right)$$

iv. the integral width $\delta_h(a, b)$ of the *h* function has the following form

$$\delta_h(a,b) = \frac{\pi}{\left(a^a b^b\right)^{1/(a+b)} \cos\left(\frac{\pi}{2}\frac{a-b}{a+b}\right)} \tag{26}$$

v. the Fourier transform of the *h* function is given by the relationship

$$H(L)=\frac{A}{2}\int_{-\infty}^{+\infty}\frac{\cosh qs'+\sinh qs'}{\cosh \rho s'}e^{-2\pi s'L}\,ds'=\frac{\pi A}{2\rho\left|\cos\left(\frac{\pi q}{2\rho}+i\frac{\pi^2 L}{\rho}\right)\right|^2}\cos\left(\frac{\pi q}{2\rho}-i\frac{\pi^2 L}{\rho}\right) \tag{27}$$

vi. if we consider the functions *f* and *g* defined by equation (25), by their deconvolution we can compute the $|F(L)|$ function, which is used in Warren and Averbach's analysis in [12]. Therefore, the magnitude of *F(L)* function has the following form:

$$\left|F(L)\right|=\frac{A_h\rho_g}{A_g\rho_h}\sqrt{\frac{\cos^2\alpha+\sinh^2\beta L}{\cos^2\gamma+\sinh^2\delta L}}, \tag{28}$$

where the arguments of trigonometric and hyperbolic functions are expressed by

$$\alpha=\frac{\pi q_g}{2\rho_g},\quad \beta=\frac{\pi^2}{\rho_g},\quad \gamma=\frac{\pi q_h}{2\rho_h},\quad \delta=\frac{\pi^2}{\rho_h}$$

The subscripts *g* and *h* refer to the instrumental and experimental XRLP. Taking into account the convolution theorem, the true sample function *f* is given by the relationship

$$f(s)=\frac{A_h\rho_g}{A_g\rho_h}\int_{-\infty}^{+\infty}\frac{\cos\left(\frac{\pi q_g}{2\rho_g}+i\frac{\pi^2 L}{\rho_g}\right)}{\cos\left(\frac{\pi q_h}{2\rho_h}+i\frac{\pi^2 L}{\rho_h}\right)}\exp(2\pi iLs)\,ds$$

The last integral cannot be accurately resolved. In order to do so we have to consider some arguments. The Fourier transform of *f* is the *F* function, given by the relations

$$F(L)=\left|F(L)\right|\exp(i\theta(L)),\quad \theta(L)=\arctan\frac{\Im\left(F(L)\right)}{\Re\left(F(L)\right)}$$

where θ means the angle function, and $\Re(F)$ and $\Im(F)$ are the real and imaginary parts of the complex function *F*, respectively. The arguments α, β, γ and δ from equation (28) depend only on the asymmetry parameters *a* and *b* of the *g* and *f* functions. If the XRLP asymmetry is not very large (i.e., *a* and *b* parameters are close enough as values) the $\cos^2\alpha \approx 1$, $\cos^2\gamma \approx 1$ approximations are reliable. Therefore, we obtain $\Im(F) << \Re(F)$, $\theta(L) \approx 0$ and the magnitude of the Fourier transform for the true XRLP sample can be expressed as

http://dx.doi.org/10.5772/59667

$$\left|F(L)\right| = \frac{A_h \rho_g}{A_g \rho_h} \frac{\cosh \frac{\pi^2 L}{\rho_g}}{\cosh \frac{\pi^2 L}{\rho_h}} \tag{29}$$

(vii) if we consider the previous approximation, the true XRLP sample is given by an inverse Fourier transform of the *F* function, and consequently we have

$$f(s') = \frac{2A_h \rho_g}{\pi A_g} \frac{\cos \frac{\pi \rho_h}{2\rho_g} \cosh \rho_h s'}{\cosh 2\rho_h s' + \cos \frac{\pi \rho_h}{\rho_g}} \tag{30}$$

(viii) the integral width of the true XRLP sample can be expressed by the δ_f function

$$\delta_f(\rho_h, \rho_g) = \frac{\pi}{2\rho_h \cos \frac{\pi \rho_h}{2\rho_g}} \left(\cos \frac{\pi \rho_h}{\rho_g} + 1 \right) \tag{31}$$

4.4. Voigt distribution applied in X-ray line profile analysis

Before briefly describing the mathematical properties of the Voigt distribution, let us examine the physical concept underlying the approximation of the XRLP by Voigt distribution and the convolution process.

During decades of research, Warren and Averbach [12] introduced the X-ray diffraction concept for the mosaic structure model, in which the atoms are arranged in blocks, each block itself being an ideal crystal, but with adjacent blocks that do not accurately fit together. They considered that the XRLP h represents the convolution between the true sample f and the instrumental function g, produced by a well-annealed sample. The effective crystallite size D_{eff} and lattice disorder parameter $<\varepsilon_{hkl}>$ were analysed as a set of independent events in a likelihood concept. Based on Fourier convolution produced between f and g signals and the mosaic structural model, the analytical form of the Fourier transform for the true sample function was obtained. The normalized *F* was described as the product of two factors, $F^{(s)}(L)$ and $F^{(\varepsilon)}(L)$, where variable *L* represents the distance perpendicular to the (hkl) reflection planes. The factor $F^{(s)}(L)$ describes the contribution of crystallite size and stocking fault probability, while the factor $F^{(\varepsilon)}(L)$ gives information about the microstrain of the lattice. The general form of the Fourier transform of the true sample for cubic lattices was given by relationships

$$F^{(s)}(L) = e^{-\frac{|L|}{D_{eff}(hkl)}}, \qquad F^{(\varepsilon)}(L) = e^{-\frac{2\pi^2 \left\langle \varepsilon_L^2 \right\rangle_{hkl} h_0^2 L^2}{a^2}}, \tag{32}$$

where $h_0^2=h^2+k^2+l^2$. The general form of the true sample function f is given by inverse Fourier transform of $F(L)$

$$f(s)=\int_{-\infty}^{\infty} e^{-\beta L^2-\gamma|L|}e^{2\pi i s L}dL= \\ =\sqrt{\frac{\pi}{\beta}}\exp\left[\frac{\gamma^2-(2\pi s)^2}{4\beta}\right]\left\{\Re\left(erfc\left(\frac{\gamma-2\pi i s}{2\sqrt{\beta}}\right)\right)\cos\frac{\pi\gamma s}{\beta}-\Im\left(erfc\left(\frac{\gamma+2\pi i s}{2\sqrt{\beta}}\right)\right)\sin\frac{\pi\gamma s}{\beta}\right\} \tag{33}$$

where $s=2\left(\frac{\sin\theta}{\lambda}-\frac{\sin\theta_0}{\lambda}\right)$, $erf(x)=\frac{2}{\sqrt{\pi}}\int_0^x e^{-t^2}dt$, $erfc(x)=1-erf(x)$ is the complementary error function [13] and $\beta=\frac{2\pi^2\langle\varepsilon_L^2\rangle_{hkl}h_0^2}{a^2}$, $\gamma=\frac{1}{D_{eff}(hkl)}$. The last relation from the mathematical point of view represents a Voigt distribution. If we take into account the properties of the Gauss and Cauchy distributions, the Voigt distribution can be generalized by relation

$$V(x,\gamma_G,\gamma_C)=\int_{-\infty}^{+\infty} I_G(x',\gamma_G,x_{0G})I_C(x-x',\gamma_C,x_{0C})dx' \tag{34}$$

Based on relation (18), its Fourier transform is given by $FT[V]=FT_{F_G}[I_G]\cdot FT_{F_C}[I_C]$ where

$$F_G(L)=e^{-2\pi i x_{0G}L_e-\pi^2\gamma_G^2L^2} \quad \text{and} \quad F_C(L)=e^{-2\pi i x_{0C}L-2\pi\gamma_C|L|}$$

The analytical expression of the Voigt distribution is

$$V(x,\gamma_G,\gamma_C)=FT^{-1}\left[e^{-2\pi i(x_{0C}+x_{0G})L}e^{-\pi^2\gamma_G^2L^2-2\pi\gamma_C|L|}\right] \tag{35}$$

Explicit forms of experimental signal and true sample function normalized at I_{0V} are given by relations [13]

$$V(x,\gamma_G,\gamma_C)=\frac{I_{0V}}{\sqrt{\pi}\gamma_G}\exp\left[\frac{\gamma_C^2-(x-x_{0C}-x_{0G})^2}{\gamma_G^2}\right]\cdot \\ \cdot\left\{\Re\left[erfc\left(\frac{\gamma_C-i(x-x_{0C}-x_{0G})}{\gamma_G}\right)\right]\cos\frac{2\gamma_C(x-x_{0C}-x_{0G})}{\gamma_G^2}-\right. \\ \left.-\Im\left[erfc\left(\frac{\gamma_C+i(x-x_{0C}-x_{0G})}{\gamma_G}\right)\right]\sin\frac{2\gamma_C(x-x_{0C}-x_{0G})}{\gamma_G^2}\right\} \tag{36}$$

http://dx.doi.org/10.5772/59667

and

$$V_f(x,\gamma_{G,f},\gamma_{C,f}) = \frac{1}{\sqrt{\pi}\gamma_{C,f}}\exp\left[\frac{\gamma_{C,f}^2-(x-x_{0C}-x_{0G})^2}{\gamma_{G,f}^2}\right]\cdot$$
$$\cdot\left\{\Re\left[erfc\left(\frac{\gamma_{C,f}-i(x-x_{0C}-x_{0G})}{\gamma_{G,f}}\right)\right]\cos\frac{2\gamma_{C,f}(x-x_{0C}-x_{0G})}{\gamma_{G,f}^2}-\right. \tag{37}$$
$$\left.-\Im\left[erfc\left(\frac{\gamma_{C,f}+i(x-x_{0C}-x_{0G})}{\gamma_{G,f}}\right)\right]\sin\frac{2\gamma_C(x-x_{0C}-x_{0G})}{\gamma_{G,f}^2}\right\}$$

Maximum value of true sample function is

$$V_{\max} = \frac{1}{\sqrt{\pi}\gamma_G}\exp\left(\frac{\gamma_C^2}{\gamma_G^2}\right)erfc\left(\frac{\gamma_C}{\gamma_G}\right)$$

Voigt function is a probability density function and it displays the distribution of target values,

$$\int_{-\infty}^{\infty}V(x,\gamma_G,\gamma_C)dx = \frac{1}{\pi\sqrt{\pi}}\frac{\gamma_C}{\gamma_G}\int_{-\infty}^{\infty}\left[\int_{-\infty}^{\infty}\frac{e^{-\left(\frac{x'}{\gamma_G}\right)^2}}{\gamma_C^2+\left(x-x'\right)^2}dx'\right]dx = 1,$$
$$\delta_V = \frac{\sqrt{\pi}\gamma_G}{\exp\left(\frac{\gamma_C}{\gamma_G}\right)^2 erfc\left(\frac{\gamma_C}{\gamma_G}\right)} \tag{38}$$

and the convolution of two Voigt functions is also a Voigt function.

The integral width of a true sample function has the two components given by the Gauss and Cauchy contributions

$$\delta_{G,f}^2 = \frac{1}{\pi}\left(\delta_{G,h}^2-\delta_{G,g}^2\right),\quad \delta_{C,f} = \frac{1}{\pi}\left(\delta_{C,h}-\delta_{C,g}\right) \tag{39}$$

Balzar and Popa are among the leading scientists in the field of Fourier analysis of X-ray diffraction profiles, and they suggested that each Gauss and Cauchy component contains information about the average crystallite size (δ_S) and distortion of the lattice (δ_D) as in [14]. From the algebraic point of view, they proposed the following relationship

$$\delta_{G,f}^2 = \delta_{SG,f}^2+\delta_{DG,f}^2,\quad \delta_{C,f} = \delta_{SC,f}+\delta_{DC,f} \tag{40}$$

Based on the new concept introduced by them, the two components of the Fourier transform are given by the relations

$$F^S(L) = e^{-\pi L^2 \delta_{SG,f}^2 - 2|L|\delta_{SC,f}}, \quad F^D(L) = e^{-\pi L^2 \delta_{DG,f}^2 - 2|L|\delta_{DC,f}} \tag{41}$$

The particle size distribution function, *P(L)* is determined from the second derivative of strain-corrected Fourier transform of the true sample function. The volume-weighted column-length P_V and surface-weighted column-length P_S distributions are given by the following [14]:

$$P_V(L) = L\frac{d^2F^S(L)}{dL^2} = 2L\left[2\left(\pi L\delta_{SG}^2 + \delta_{SC}\right)^2 - \pi\delta_{SG}^2\right]F^S(L) \tag{42}$$

$$P_S(L) = P_V(L) = \frac{d^2F^S(L)}{dL^2} = 2\left[2\left(\pi L\delta_{SG}^2 + \delta_{SC}\right)^2 - \pi\delta_{SG}^2\right]F^S(L) \tag{43}$$

5. Experimental section, data analysis and results

A series of four supported gold catalysts were studied by X-ray diffraction (XRD) in order to determine the average particle size of the gold, the microstrain of the lattice as well as the size and microstrain distribution functions by XRLP deconvolution using Fourier transform technique. The gold catalyst samples with up to 5 wt% gold content were prepared by impregnation of the SiO_2 support with aqueous solution of $HAuCl_4 \times 3H_2O$ and homogeneous deposition-precipitation using urea as the precipitating agent method, respectively. The X-ray diffraction data of the supported gold catalysts displayed in Figure 3 were collected using a Rigaku horizontal powder diffractometer with rotated anode in Bragg-Brentano geometry with Ni-filtered Cu Kα radiation, $\lambda = 1.54178$ Å, at room temperature. The typical experimental conditions were: 60 sec for each step, initial angle $2\theta = 32^0$, and a step of 0.02^0, and each profile was measured at 2700 points. The XRD method is based on the deconvolution of the experimental XRLP (111) and (222) using Fourier transform procedure by fitting the XRLP with the Gauss, Cauchy, GFF and Voigt distributions. The Fourier analysis of XRLP validity depends strongly on the magnitude and nature of the errors propagated in the data analysis. The scientific literature treated three systematic errors: uncorrected constant background, truncation, and effect of sampling for the observed profile at a finite number of points that appear in discrete Fourier analysis. In order to minimize propagation of these systematic errors, a global approximation of the XRLP is adopted instead of the discrete calculus. The reason for this choice was the simplicity and mathematical elegance of the analytical Fourier transform magnitude and the integral width of the true XRLP given by equations (20)-(24), (31), (34) and (38), as in [15]. The robustness of these approximations for the XRLP arises from the possibility of using the analytical forms of the Fourier transform instead of a numerical fast Fourier transform (FFT). It is well known that the validity of the numerical FFT depends drastically

http://dx.doi.org/10.5772/59667

on the filtering technique what was adopted in [16]. In this way, the validity of the nanostructural parameters is closely related to the accuracy of the Fourier transform magnitude of the true XRLP.

Experimental relative intensities (111) with respect to 2θ values for (1) system are shown in Figure 4. The next steps consist in background correction of XRLP by polynomial procedures, finding the best parameters for the distributions adopted using the method of least squares or nonlinear fit, and then deconvoluting them using instrumental function. The main steps in the data analysis of the investigated systems are shown in Figure 4.

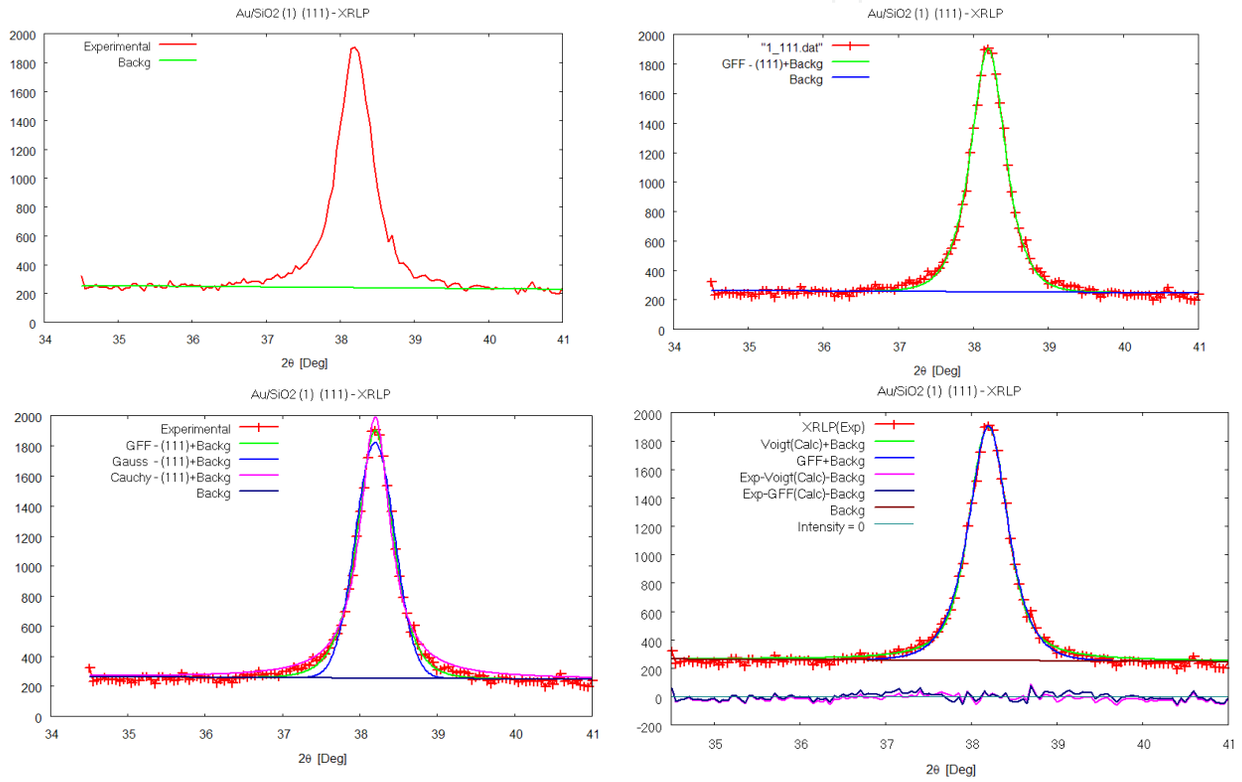

Figure 4. Various stages of processing for X-ray line profile (111) of the sample (1)

Experimental relative intensities (222) with respect to 2θ values for (6) system are shown in Figure 5.

The Fourier transforms normalized for the true sample function of the investigated samples (1) and (6) were calculated by three distinct methods, based on relations (28), (32) and (41), and are displayed in Figure 6.

The microstrain and particle size distribution functions determined by Fourier deconvolution of a single XRLP were calculated using equation (32), and are plotted in Figure 7.

The credibility of the parameters describing the investigated nanostructure systems depends primarily on the process of approximation of XRLP. This criterion is expressed by the root mean squares of residuals (*rmsr*) of data analysis and is given by relation

$$rmsr = 100\sqrt{\frac{\sum_{i=1}^{N_{\text{points}}} \frac{\left(y_i^{calc} - y_i^{\exp}\right)^2}{\sigma_i^2}}{N_{\text{points}} - N_{param}}}$$

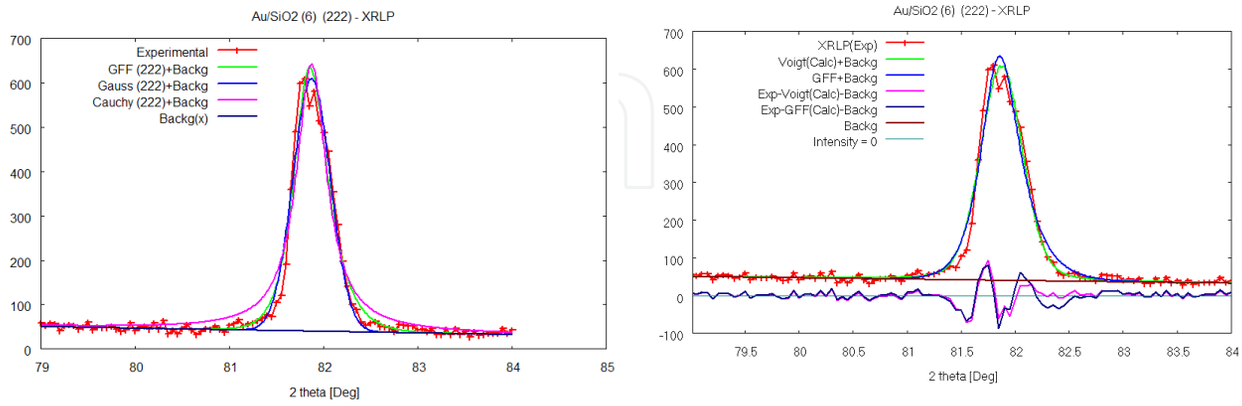

Figure 5. Various stages of processing for X-ray line profile (222) of the sample (6)

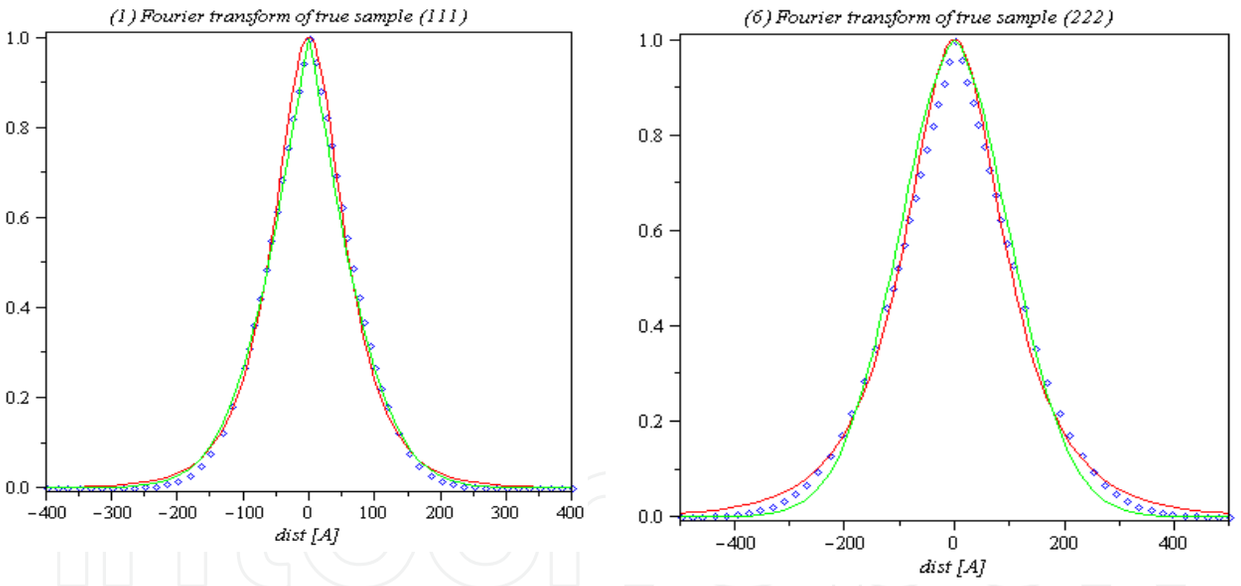

Figure 6. Fourier transform of true sample function of XRLP (111) and (222) for systems (1) and (6): blue - general relation, red - GFF, green - Voigt distribution

The *rmsr* values for all distributions used in XRLP approximation process are given in Table 1. The *rmsr* values are closely related to the spectral noise of experimental data. Here it is shown that a model based on GFF and Voigt distribution may be more realistic and accurate.

The integral widths and FWHM of the true sample functions calculated for all distributions were determined using the relations (21), (23), (31) and (38). Their values are presented in Table 2.

http://dx.doi.org/10.5772/59667

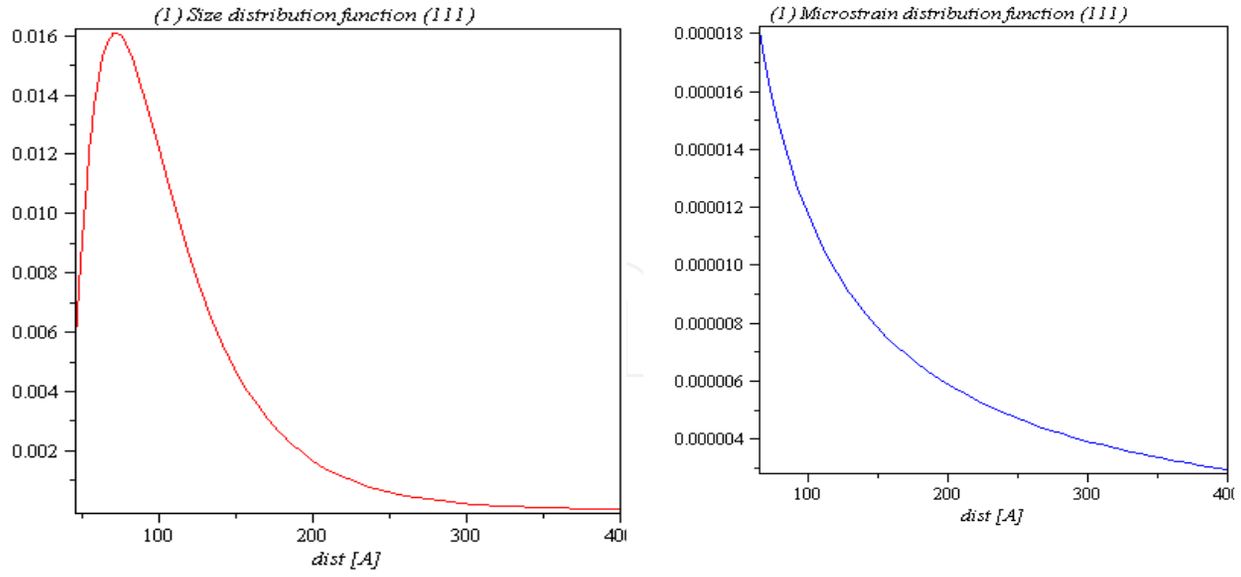

Figure 7. Size and microstrain distribution functions of (111) XRLP for system (1)

Sample	hkl	Distribution			
		GFF	Gauss	Cauchy	Voigt
(1)	111	26.2658	47.6477	40.6091	26.9398
	222	14.8795	15.2648	16.0429	15.1880
(3)	111	21.5743	31.4428	28.0142	22.1633
	222	12.5725	12.4615	12.6212	12.4534
(5)	111	18.1273	26.6941	21.8148	17.4276
	222	13.2033	13.3122	13.2599	13.2771
(6)	111	28.1267	31.8679	36.0040	35.5948
	222	18.8487	20.5945	33.2718	19.9656

Table 1. Values for *rmsr* for investigated samples

Because the experimental XRLP was measured for both (111) and (222), the surface-weighted column-length P_S and volume-weighted column-length P_V distribution functions were determined using relations (42,43) implemented in BREADTH software [17]. Additionally, it has found that the Gumbel distribution is the most adequate function for the global approximation of both probabilities' curves, and the results are shown in Figure 8.

The global structural parameters obtained for the investigated samples are summarized in Table 3 and Table 4.

Sample	hkl	2θ⁰ [Deg]	Distributions							
			GFF		Gauss		Cauchy		Voigt	
			δ [Deg]	a* [Deg]	δ [Deg]	a* [Deg]	δ [Deg]	a* [Deg]	δ [Deg]	a* [Deg]
(1)	111	38.291	0.644	0.540	0.638	0.599	0.738	0.469	0.713	0.537
	222	81.780	0.862	0.715	0.854	0.803	1.025	0.653	0.927	0.765
(3)	111	38.220	0.802	0.672	0.798	0.750	0.919	0.585	0.891	0.668
	222	81.763	1.028	0.860	1.011	0.950	1.181	0.752	1.095	0.912
(5)	111	38.211	0.631	0.529	0.621	0.583	0.723	0.460	0.701	0.519
	222	81.801	1.052	0.873	1.067	1.003	1.225	0.780	1.185	0.890
(6)	111	38.292	0.363	0.304	0.363	0.341	0.426	0.271	0.374	0.335
	222	81.872	0.506	0.423	0.498	0.468	0.613	0.390	0.528	0.461

a* represents FWHM

Table 2. Values for integral width and full width at half maximum for investigated samples

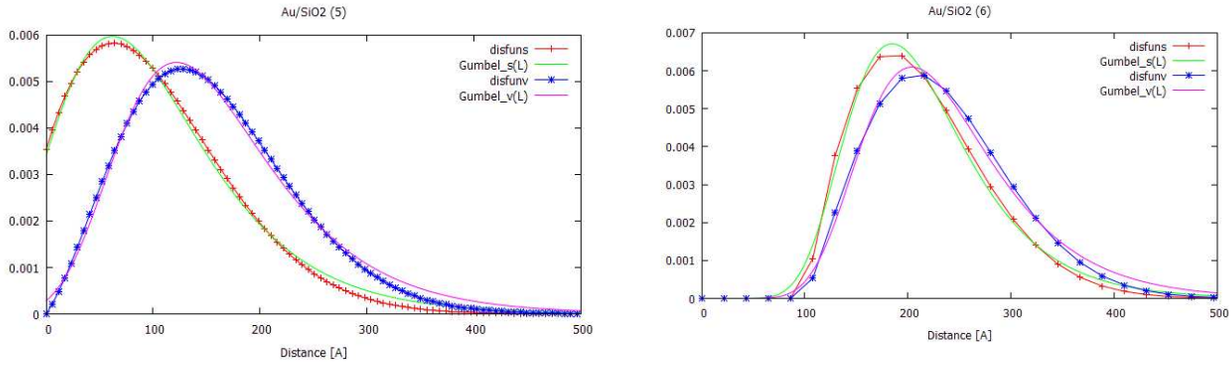

Figure 8. Surface-weighted column-length distribution function, $P_{S,}$ and volume-weighted column-length distribution function, $P_{V,}$ for (5) and (6) systems

Sample	GFF approximation				Single Voigt approximation			
	D_{111}^{Sch}	D_{111}	D_{222}^{Sch}	D_{222}	D_{111}^{Sch}	D_{111}	D_{222}^{Sch}	D_{222}
(1)	180	168	180	139	145	154	118	145
(3)	143	135	139	130	116	118	98	139
(5)	183	171	145	112	153	151	108	95
(6)	398	309	313	263	249	384	199	303

Table 3. Values for crystallite size determined by Scherrer method, and effective crystallite size using single XRLP approximations

Sample	hkl	$\langle D\rangle_S \pm \Delta D_S$ [Å]	$\langle D\rangle_V \pm \Delta D_V$ [Å]	$\langle \varepsilon^2(D_V/2)\rangle^{1/2} \pm \Delta\langle \varepsilon^2(D_V/2)\rangle^{1/2}$
(1)	[111/222]	90±12	133±15.	0.211E-02 ± 0.152E-03
(3)	[111/222]	69±13	104± 17	0.262E-02 ± 0.288E-03
(5)	[111/222]	106±30	153±41	0.280E-02 ± 0.216E-03
(6)	[111/222]	214±72	233±79	0.105E-02 ± 0.522E-03

Table 4. Values for the average crystallite size and microstrain using double Voigt approaches

Hydrogen chemisorption, transmission electron microscopy (TEM), magnetization, electronic paramagnetic resonance (EPR) and other methods could also be used to determine the average diameter of particles by taking into account a prior spherical form for the grains. By XRD method we can obtain the crystallite sizes that have different values for different crystallographic planes. There is a large difference between the particle size and the crystallite size due to the different physical meaning of the two concepts. It is possible that the particles of the supported gold catalysts are made up of many gold crystallites.

The size of the crystallites determined by equations (32) and (41), corresponding to (111) and (222) planes, have different values. The crystallite sizes D_{111}^{Sch} and D_{222}^{Sch} are determined by the Scherrer method [18] without taking into account the microstrain of the lattice. The values D_{111} and D_{222} were determined by Fourier deconvolution method for single XRLP, while the averages of D_V and D_S were calculated by a double Voigt approach. The difference between the crystallites' size can be explained by the fact that the analytical models are different due to the different approaches. This means that the geometry of the crystallites is not spherical [18]. The microstrain parameter of the lattice can also be correlated with the effective crystallite size in the following way: the value of the effective crystallite size increases when the microstrain value decreases.

The main procedures of the SIZE.mws software dedicated to Fourier analysis of the XRLP by GFF and Voigt distributions written in Maple 11 language are presented in Appendix 2.

6. Conclusions

In the present chapter, it is shown that XRD analysis provides more information for understanding the physical properties of nanomaterial structure. Powder X-ray diffraction is the cheapest and most reliable method compared with hydrogen chemisorptions, TEM techniques, magnetic measurements, EPR, etc. The main conclusions that can be drawn from these studies are:

1. For XRLP analysis, a global approximation should be applied rather than a numerical Fourier analysis. The former analysis is better than a numerical calculation because it can minimize the systematic errors that could appear in the traditional Fourier analysis.
2. Our numerical results show that by using the GFF and the Voigt distribution we successfully obtained reliable global nanostructural parameters;

3. Cauchy and Gauss distributions used for XRLP approximation give roughly structural information;

4. Powder X-ray diffraction gives the most detailed nanostructural results, such as: average crystallite size, microstrain, and distribution functions of crystallite size and microstrain;

5. Surface-weighted domain size depends only on Cauchy integral breadth, while volume-weighted domain size depends on Cauchy and Gauss integral breadths;

6. To obtain valid structural results, it is important to have: a good S/N ratio of the experimental spectra, a good deconvolution technique for the experimental and instrumental spectra, and an adequate computer package and programs for data analysis.

Appendix 1

Input data h.txt and g.txt files

```
`k`:=1;
line_h:= readline(`h.txt`):
line_g:= readline(`g.txt`):
while line <> 0 do
temp_h:= sscanf(line_h,`%8f%8f`):temp_g:=sscanf(line_g,`%8f %8f`):
printf(`%10.5f %10.5f`,temp_h[1],temp_h[2]): lprint():
printf(`%10.5f %10.5f`,temp_g[1],temp_g[2]): lprint():
twotheta_h[`k`]:=temp_h[1];
intensity_h[`k`]:=temp_h[2];
twotheta_g[`k`]:=temp_g[1];
intensity_g[`k`]:=temp_g[2];
line_h:= readline(`h.txt`):
line_g:= readline(`g.txt`):
`k`:=`k`+1;
end do;
`k`:=`k`-1;
p_h:=plot([twotheta_h[`ih`],intensity_h[`ih`],`ih`=1..k],col-
or=red,style=LINE,thickness=2,axes=boxed,gridlines,
labels=["2theta",""]):
p_g:=plot([twotheta_g[`ig`],intensity_g[`ig`],`ig`=1..k],col-
or=blue,style=LINE,thickness=2,axes=boxed,gridlines,
labels=["2theta",""]):
display({p_h,p_g});
deltatwotheta:=twotheta_h[2]-twotheta_h[1]:
```

h vector determination

```
twok:=2*k;
for `i` from 1 to k
do
h[`i`]:=intensity_h[`i`]:
end do:
```

http://dx.doi.org/10.5772/59667

```
h[`k`+1]:=0:
`j`:=1:
for `i` from `k`+2 to twok+1
do
h[`i`]:=intensity_h[`j`]:
`j`:=`j`+1:
end do:
print(h);
```

g array determination

```
`j`:=1:
for `i` from -twok to -k
do
g[`i`]:=intensity_g[`j`]:
`j`:=`j`+1;
end do:
`j`:=1:
for `i` from -k to -1
do
g[`i`]:=intensity_g[`j`]:
`j`:=`j`+1:
end do:
g[0]:=0.:
for `i` from 1 to k
do
g[`i`]:=intensity_g[`i`]:
end do:
`j`:=1:
for `i` from k+1 to twok
do
g[`i`]:=intensity_g[`j`]:
`j`:=`j`+1:
end do:
print(g):
```

a matrix determination

```
for `i` from 1 to twok+1
do
for `j` from 1 to twok+1
do
a[`i`,`j`]:=0.:
end do:
end do:
`i1`:=0:
for `i` from -k to k
do
`j1`:=0:
`i1`:=`i1`+1:
for `j` from -k to k
do
```

```
`j1`:=`j1`+1:
a[`i1`,`j1`]:=g[`i`-`j`]*deltatwotheta;
end do:
end do:
print(a);
```

solving integral deconvolution equation by direct discretization

```
f:=linsolve(a,h):
for `i` from 1 to twok+1
do
twotheta_f[`i`]:=twotheta_h[1]+(`i`-1)*deltatwotheta:
intensity_f[`i`]:=eval(f[`i`]);
end do:
p_h:=plot([twotheta_h[`ihh`],intensity_h[`ihh`],`ihh`=1..k],col-
or=red,style=LINE,thickness=2,axes=boxed,gridlines,labels=["2theta",""]):
p_g:=plot([twotheta_g[`igg`],intensity_g[`igg`],`igg`=1..k],
color=blue,style=LINE,thickness=2,axes=boxed,gridlines,
labels=["2theta",""]):
p_f:=plot([twotheta_f[`iff`],intensity_f[`iff`],`iff`=1..twok+1],
color=green,style=LINE,thickness=2,axes=boxed,gridlines,
labels=["2theta",""]):
display({p_h,p_g,p_f});
fd:= fopen("f",WRITE,TEXT):
for `i` from 1 to k
do
fprintf(fd,"%g %g\n",twotheta_f[`i`],intensity_f[`i`]):
end do:
fclose(fd):
```

Appendix 2

Fourier transform of true sample function procedure

```
f_GFF_freq:=proc(freq)
local arg_in,arg_sa;
arg_in:=(Pi*q_in)/(2*rho_in) + I *(Pi*Pi*freq)/rho_in;
arg_sa:=(Pi*q_sa)/(2*rho_sa) + I * (Pi*Pi*freq)/rho_sa;
(ampl_sa/ampl_in)*(rho_in/rho_sa)*cos(arg_in)/cos(arg_sa);
end:
```

Module of Fourier transform of true sample function procedure

```
FT_GFF_modul:=proc(freq)
local aux,bux,auxr_0,auxi_0;
aux:=evalc(Re(f_GFF_freq(freq))):
bux:=evalc(Im(f_GFF_freq(freq))):
aux:=aux*aux+bux*bux:
auxr_0:=evalc(Re(f_GFF_freq(0))):
auxi_0:=evalc(Im(f_GFF_freq(0))):
```

```
bux:=auxr_0*auxr_0+auxi_0*auxi_0:
sqrt(aux/bux):
end:
```

True sample function procedure

```
f_GFF_s:=proc(s)
local arg1,arg2;
arg1:=(Pi/2)*(rho_sa/rho_in);
arg2:=(rho_sa*s);
(2/Pi)*(ampl_sa/ampl_in)*
rho_in*cos(arg1)*cosh(arg2)/(cosh(2*arg2)+cos(2*arg1));
end:
```

Integral width of true sample function procedure

```
int_width_GFF:=proc(rho_in,rho_sa)
local arg;
arg:=Pi*rho_sa/rho_in;
Pi/(2*rho_sa*cos(arg/2))*(cos(arg)+1);
end:
```

Moment of zero order for experimental X-ray line profile procedure

```
mu_0_GFF:=proc(ampl,rho,q)
local arg;
arg:=(Pi*q)/(2*rho);
(ampl/2)*(Pi/rho)*(1/cos(arg));
end:
```

Moment of first order for experimental X-ray line profile procedure

```
mu_1_GFF:=proc(rho,q)
local arg;
arg:=(Pi*q)/(2*rho);
(Pi/(2*rho))*tan(arg);
end:
```

Moment of second order for experimental X-ray line profile procedure

```
mu_2_GFF:=proc(rho,q)
local arg;
arg:=(Pi*q)/(2*rho);
((Pi/(2*rho))^2)*(1./(cos(arg)^2)+tan(arg)^2);
end:
```

Experimental X-ray line profile procedure approximated by GFF distribution

```
exp_profile_GFF:=proc(s)
local arg_q,arg_rho;
arg_q:=q*s; arg_rho:=rho*s;
(ampl/2)*(cosh(arg_q)+sinh(arg_q))/cosh(arg_rho);
end:
```

Instrumental X-ray line profile procedure determined by GFF distribution

```
inst_profile_GFF:=proc(s)
local arg_q,arg_rho;
arg_q:=q_in*s; arg_rho:=rho_in*s;
(ampl_in/2)*(cosh(arg_q)+sinh(arg_q))/cosh(arg_rho);
end:
```

Fourier transform procedure for general relation of true sample function developed by Warren-Averbach theory

```
gen_function:=proc(freq)
exp(-beta_gen(fmin,fmax)*freq*freq-
gama_gen(fmin,fmax)*abs(freq));
end:
```

Procedure for experimental XRLP given by Voigt approximation

```
h_Voigt_function:=proc(s)
local arg1,arg2,arg3,arg4;
arg1:=(gama_h_c**2-s**2)/(gama_h_g**2);
arg2:=(gama_h_c-I*s)/gama_h_g;
arg3:=(gama_h_c+I*s)/gama_h_g;
arg4:=2.*gama_h_c*s/(gama_h_g**2);
amp_h/(sqrt(Pi)*gama_h_g)*exp(arg1)*
(Re(erfc(arg2))*cos(arg4)-Im(erfc(arg3))*sin(arg4));
end:
```

Procedure for instrumental XRLP given by Voigt approximation

```
g_Voigt_function:=proc(s)
local arg1,arg2,arg3,arg4;
arg1:=(gama_g_c**2-s**2)/(gama_g_g**2);
arg2:=(gama_g_c-I*s)/gama_g_g;
arg3:=(gama_g_c+I*s)/gama_g_g;
arg4:=2.*gama_g_c*s/(gama_g_g**2);
amp_g/(sqrt(Pi)*gama_g_g)*exp(arg1)*
(Re(erfc(arg2))*cos(arg4)-Im(erfc(arg3))*sin(arg4));
end:
```

Procedure for the true sample function calculated by Voigt approximation

```
f_Voigt_function:=proc(s)
local arg1,arg2,arg3,arg4;
arg1:=(gama_f_c**2-s**2)/(gama_f_g**2);
arg2:=(gama_f_c-I*s)/gama_f_g;
arg3:=(gama_f_c+I*s)/gama_f_g;
arg4:=2.*gama_f_c*s/(gama_f_g**2);
amp_h/amp_g/(sqrt(Pi)*gama_f_g)*exp(arg1)*(Re(erfc(arg2))*cos(arg4)-
Im(erfc(arg3))*sin(arg4));
end:
```

Acknowledgements

Financial support received from the European Union through the European Regional Development Fund, Project ID 1822/SMIS CSNR 48797 CETATEA, is gratefully acknowledged. In particular, one of the topics covered by the book *Fourier Transform of the Signals* will be a useful starting point in accomplishing one of its major objectives, energy recovery from ambient pollution. Additionally, the authors are grateful to the staff of Beijing Synchrotron Radiation Facilities for beam time and for their technical assistance in XRD measurements.

Author details

Adrian Bot[1], Nicolae Aldea[1*] and Florica Matei[2]

*Address all correspondence to: naldea@itim-cj.ro

1 National Institute for Research and Development of Isotopic and Molecular Technologies, Cluj-Napoca, Romania

2 University of Agricultural Sciences and Veterinary Medicine, Cluj-Napoca, Romania

References

[1] Kabanikin S. Inverse and Ill-Posed Problems: Theory and Applications. Berlin/ Boston: Walter de Gruyter GmbH; 2011.

[2] Nedelcov I. P. Improper Problems in Computational Physics. Computer Physics Communications 1972; 4(2)157-163.

[3] Read R. J. Intensity Statistics in the Presence of Translational Noncrystallographic Symmetry. Acta Crystallographica Section D 2013; 69(2) 176-183.

[4] Kleefeld A., Cottbus B. T. U. Numerical Results for Linear Fredholm Integral Equations of the First Kind over Surfaces in 3D. International Journal of Computer Mathematics 2010; 1(1) 1-16.

[5] Naumova V., Pereverzyev S. V. Multi-penalty Regularization with a Component-wise Penalization. Inverse Problems 2013; 29(7) 1-16.

[6] Kabanikin S., editor. Regularization Theory for Ill-posed Problems: Selected Topics. Inverse and Ill Posed Problems Series 58. Berlin/Boston: Walter de Gruyter GmbH; 2013.

[7] Beniaminy I., Deutsch M. A Spline Based Method for Experimental Data Deconvolution. Computer Physics Communications 1980; 21(2): 271-277.

[8] Fredrikze H., Verkerk P. Comment on "A spline based method for experimental data deconvolution". Computer Physics Communications 1981; 24(1), 5-7.

[9] Aldea N., Tiusan C., Zapotinschi R. A New Approach Used to Evaluation the Crystallite Size of Supported Metal Catalysts by Single X-Ray Profile Fourier Transform Implemented on Maple V. In: Borcherds P., Bubak M., Maksymowicz A., editors. 8th Joint EPS-APS International Conference on Physics Computing, PC '96 17-21 September 1996, Krakow: Academic Computer Centre CYFRONET-KRAKOW; 1996.

[10] Balzar D., Ledbetter H. J. Voigt-Function Modeling in Fourier-Analysis of Size and X-ray Diffraction Peaks-Peaks. Journal of Applied Crystallography 1993; 26(1) 97-103.

[11] Aldea N., Gluhoi A., Marginean P., Cosma C., Yaning X. Extended X-Ray Absorption Fine Structure and X-Ray Diffraction Studies on Supported Nickel Catalysts. Spectrochimica Acta Part 2000; 55(7) 997-1008.

[12] Aldea N., Barz B., Pintea S., Matei F. Theoretical Approach Regarding Nanometrology of the Metal Nanoclusters Used in Heterogeneous Catalysis by Powder X-Ray Diffraction Method. Journal of Optoelectronics and Advanced Materials 2007; 9(10) 3293-3296.

[13] Gradstein I. S., Rijik L. M. Tables of Integrals, Sums, Series, and Products. Moscow: Fizmatgiz; 1962.

[14] Balzar D., Popa N. C. Crystallite Size and Residual Strain/Stress Modeling in Rietveld Refine. In: Meittemeijer E. J., Scardi P., editors. Diffraction Analysis of the Microstructure of Materials. Berlin Heidelberg New York: Springer-Verlag; 2003, pp. 125-144.

[15] Lazar M., Valer A., Pintea S., Barz B., Ducu C., Malinovschi V., Xie Yaning Aldea N. Preparation and Structural Characterization by XRD and XAS of the Supported Gold Catalysts. Journal of Optoelectronics and Advanced Materials 2008; 10(9) 2244-2251.

[16] Walker J. S. Fast Fourier Transform. 2nd ed. New York, London, Tokyo: Boca Raton CRC; 1997.

[17] Balzar D. *BREADTH-* a Program for Analyzing Diffraction Line Broadening. Journal of Applied Crystallography 1995; 28(2) 244-245.

[18] Rednic V., Aldea N., Marginean P., Rada M., Bot A., Zhonghua W., Zhang J., Matei F. Heat Treatment Influence on the Structural Properties of Supported Ni Nanoclusters. Metals and Materials International 2014; 20(4) 641-646.